Optimal Parameter Estimation for the Online Control of Ion Milling Etch Depth

Eric J. Klein and W. Fred Ramirez
Dept. of Chemical Engineering, University of Colorado, Boulder, CO 80309

The use of optimal parameter estimation for the online regulation of final etch depth in an ion milling process is described. A model-based control system utilizes a 3-D surface evolution model to predict dynamic surface profiles and etch depth. A heterodyne laser interferometer is used to measure trench height in situ for calculation of the difference in etch rates between the photoresist layer and the exposed portion of the underlying substrate layer. Adaptive material-specific etch rate parameters and operating parameters such as ion beam strength and angle of incidence are estimated optimally with an extended Kalman filter. Optimal estimates of the in situ etch depth are calculated from the adaptive model, allowing the stopping time of the milling process to be varied from run to run to regulate final etch depth in the presence of disturbances. The system installed on an ion milling machine shows that the controller is capable of accurately regulating final etch depth in the presence of large process faults.

Introduction

Trends in the microelectronics industry are quickly moving towards smaller component geometries, higher component densities, larger wafer sizes, and lower overall costs. Given these trends and the inherently tight product specifications, automatic process control is becoming an increasingly important issue (Kim et al., 1992; Edgar et al., 2000).

The etching process is a critical step in the manufacturing process. It is not uncommon for a single wafer to be etched several times at various stages of the fabrication line. Traditional wet etching processes are being replaced by ion milling due to its reduced process time, ability to etch smaller dimensions, and increased degree of anisotropy (uni-directional etching leading to the formation of vertical side walls). The ion mill, which operates by bombarding the wafer surface with accelerated, subnanometer sized ion particles, exhibits nearly vertical side walls and a ten-fold reduction in process time when compared to wet etching techniques (Lostimolo, 1995).

Current industrial practice is to operate the ion milling process in the open-loop mode. Statistical process control (SPC) is employed to monitor the quality of the finished product. However, due to the batch nature and fairly fast run times of the milling process (typically 5–10 min), it is possible that a fairly large quantity of nonconforming parts can be fabricated prior to the detection of a process fault. The rework and/or scrapping of these defective parts is costly and can cause a significant decrease in the overall yield of the fabrication line. Process faults can arise from disturbances in operating states such as beam strength and incidence angle in the milling process. Furthermore, undetected process faults from previous manufacturing steps (that is, thin-layer deposition and photo-lithography processes), which result in deviations in the physical properties of the materials being milled, seriously alter the performance of the ion milling process.

Closed-loop operation of the ion milling process is highly desirable. The control is inherently bang-bang as the only available control action is the on/off state of the ion beam. A properly designed automatic process control system will provide for the immediate detection of process faults and will allow precise control of final etch depth by manipulating the final milling time on a run to run basis. This will significantly reduce under-mill errors and the need for over-milling, thus decreasing rework and cycle time and increasing both process yield and production rate.

This article details the design of an automatic control system for regulating final etch depth in the ion milling process. The control system is based on an etch rate model and a 3-D model prediction of wafer surface evolution during the milling

Correspondence concerning this article should be addressed to W. F. Ramirez.

process (Klein and Ramirez, 2000). Heterodyne interferometry has been identified as a promising tool for monitoring surface profiles on-line. The availability of *in situ* surface profiles facilitates the calculation of the difference in etch rates between the photoresist and substrate layers. A common-path heterodyne interferometer which rejects noise caused by sample vibration has been designed for this application and is discussed elsewhere (Klein et al., 2000). An adaptive state and parameter estimation scheme using an extended Kalman filter is developed to correct the predictive model for mismatches between model predictions and the *in situ* etch rate measurement. Case studies investigating the robustness of the adaptive control scheme using simulated measurements are presented, as is a case study detailing the on-line implementation of the etch depth controller.

Controller Design

An automatic control system is designed to facilitate the on-line control of etch depth in the ion milling system (Figure 1). The system is composed of a model for predicting etch rates based on system states and material-specific etch rate parameters, a heterodyne laser interferometer for measuring the surface profiles initially and *in situ*, and an extended Kalman filter which is used for making optimal estimates of model parameters. The optimally estimated operating and material-specific etch rate parameters are used by the surface evolution model, where the optimal estimates of etch rates are propagated in three dimensions. The resulting optimal estimates of the surface profiles are used to determine the *in-situ* etch depth into the substrate layer. This allows for the on-line adjustment of the final milling time and thus the tight regulation of final etch depth.

The crucial components of the control system are the etch rate model and the 3-D surface evolution model (see next sub-section). The etch rate model uses operating parameters and material-specific etch rate parameters to predict the etch rates of both the photoresist layer and the exposed portion of the underlying substrate layer. The surface evolution model uses these etch rates to update the initial surface profiles of both the photoresist layer and the exposed portion of the underlying substrate layer, providing an accurate prediction of dynamic surface profiles during the milling process.

A heterodyne laser interferometer for the *in situ* monitoring of surface profiles during ion milling has been designed (as will be discussed later). Heterodyne laser interferometry has previously been identified as a useful tool for surface profilometry in the presence of sample vibration (Huang, 1984; Riza, 1996). This optical profilometry technique is used to accurately measure initial surface profiles which are required by the surface evolution model (Klein and Ramirez, 2000). In addition, through repeated surface profiling during the milling process, the relative difference in the etch rates of the photoresist and the underlying substrate material can be determined *in situ*. A real-time measurement of this differential etch rate is required to correct the model parameters for mismatch between the surface evolution model predictions and the state of the physical system. Possible causes of this model mismatch could include, but are not limited to, errors in the initial estimates of material-specific model parameters, as well as fluctuations or sustained deviations from nominal values in the operating states.

An extended Kalman filter state estimator is employed to provide optimal estimates of the adaptive model parameters based on etch rate model predictions and the *in situ* differential etch rate measurement (as will be discussed later). Corrected surface evolution model predictions of etch depth based on these optimally estimated parameters are compared with the desired final etch depth of the milling process, and milling continues until the specified etch depth is reached. This run to run adjustment of the final milling time immediately corrects the system for process faults, providing for the precise regulation of the final etch depth.

Etch rate and surface evolution models

The modeling of the ion milling system has been investigated by several researchers. Both 2-D (Hamaguchi et al., 1993; Arnold et al., 1994; Hamaguchi and Dalvie, 1994) and 3-D (Smith and Walls, 1980; Katardjiev, 1988; Katardjiev et al., 1990) surface evolution models have been developed and are described in the literature.

The model employed in the control system design uses the above referenced modeling approaches as a starting point and details a solution to the problem of accounting for local shadowing effects. Shadowing effects become important in high

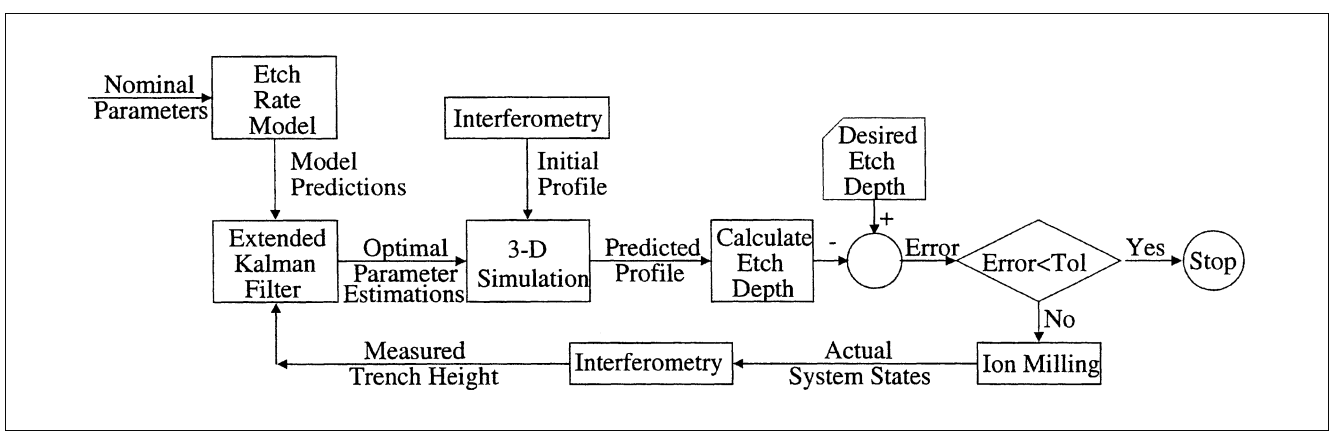

Figure 1. Automatic ion milling etch depth control system.

aspect ratio (height of photoresist/line width) applications where parts of the trench floor may be hidden from the ion beam by the photoresist layer. In addition, the basic model has been modified to account for the effects of beam voltage and wafer rotation. The practice of rotating the wafer in the azimuth plane allows for the fabrication of symmetric parts even though beam incidence angles other than normal are frequently used to increase etch rates in the ion milling process. The complete model formulation is detailed elsewhere (Klein and Ramirez, 2000) and only a brief overview is presented here.

Wafers are placed on a water-cooled milling table, which is rotated in the azimuth plane during milling to ensure symmetric surface profiles. The ion beam is incident in the direction of unit vector $\bar{\boldsymbol{n}}^1$. The outward pointing surface normal $\bar{\boldsymbol{n}}$ and, therefore, the local angle of beam incidence ϕ vary both spatially and temporally with the evolving surface profile.

The surface function S is defined to be a function of the three spatial variables in Cartesian coordinates (x, y and z) and time (t) such that

$$S(x,y,z,t) = 0 \tag{1}$$

The flux equation for surface evolution can be found by taking the total derivative of Eq. 1 to yield

$$\frac{dS}{dt} = S_x \frac{dx}{dt} + S_y \frac{dy}{dt} + S_z \frac{dz}{dt} + S_t = 0 \tag{2}$$

where subscripts denote partial derivatives. Defining c to be the vertical outward pointing surface velocity (etch rate), the final model formulation can be shown to be

$$S_t + c\sqrt{S_x^2 + S_y^2 + S_z^2} = 0 \tag{3}$$

This equation is a first-order partial differential equation belonging to the class of equations known as the Hamilton-Jacobi equations. Integration of the model is accomplished through the use of the method of characteristics.

It is well known that the ion milling etch rate c is given by the following expression (Katardjiev et al., 1988a,b; Katardjiev, 1989)

$$c = -\frac{J}{N} Y(\phi)\cos\phi \tag{4}$$

where J is ion beam current density (ions/cm^2), Y is the sputtering yield function (atoms sputtered/incident ion), and N is the atomic density of the material (atoms/cm^3).

The empirical functionality of the yield function Y is modified here to account for the effects of beam voltage (V) as follows

$$Y(\phi,V) = Y(\phi)Y^*(V) \tag{5}$$

$$Y^*(V) = \frac{Y(V)}{Y(V_{\text{ref}})} \tag{6}$$

where V_{ref} is the reference voltage at which $Y(\phi)$ is determined. The following functionalities for the components of the yield function have been hypothesized and confirmed through experimentation (Klein and Ramirez, 2000)

$$Y(\phi) = \sum_{i=1}^{4} a_i \cos^i\phi \tag{7}$$

$$Y^*(V) = b_1 V^2 + b_2 V + b_3 \tag{8}$$

where parameters **a** and **b** are material-specific model parameters which are initially determined experimentally and are updated on-line through the use of an extended Kalman filter estimator. Local surface shadowing is dealt with by determining which portions of the wafer surface are hidden from the ion beam at each time step in the simulation. This is accomplished through geometric considerations, taking into account local surface profiles, as well as the direction of the incoming ion beam (Klein and Ramirez, 2000).

In situ differential etch rate measurement

Existing analytical techniques for end-point detection and etch rate monitoring in sputtering processes are described in the literature. These techniques include end-point detection methods such as sputtered ion mass spectrometry (SIMS) (Harriott and Vasile, 1989; Beall et al., 1991; Humphreys et al., 1992), as well as laser interferometry techniques for the continuous measurement of surface displacement (Heimann and Schutz, 1984; Heinrich and Hoffmann, 1993; Smith and Walls, 1980; Veillard, 1993; Benson et al., 1996). The interferometry based techniques are far superior to the SIMS based techniques since they are capable of monitoring surface position within a single, uniform material layer, whereas SIMS allows the determination of the material layer currently being milled, but provides no information on the depth that has been etched into a homogeneous material layer.

In order to monitor etch rates *in situ* during the ion milling process, a high resolution technique capable of damping out vibrational noise caused by the rotation of the milling table is required. Heterodyne (dual-frequency) interferometers exhibit nanometer scale resolution and can be designed to dampen out sample vibration through the use of a common-path scheme where the reference and measurement arms, which are of slightly different frequencies, are simultaneously focused on the sample (Huang, 1984; Riza, 1996).

A common-path heterodyne interferometer for surface profilometry has been designed and tested (Klein et al., 2000). Detailed 2-D depictions of the surface profile can be obtained by raster scanning the measurement beam across the area of interest on the wafer surface and monitoring the phase difference between the reflected reference and measurement beams. This device is used to generate the initial surface profile required by the surface evolution model.

Furthermore, it is possible to make use of the fact that in ion milling processes, in contrast to wet etching processes where the photoresist is chemically resistant to the etching medium, both the photoresist layer and the exposed portions of the substrate layer are etched. The etch rates of the layers

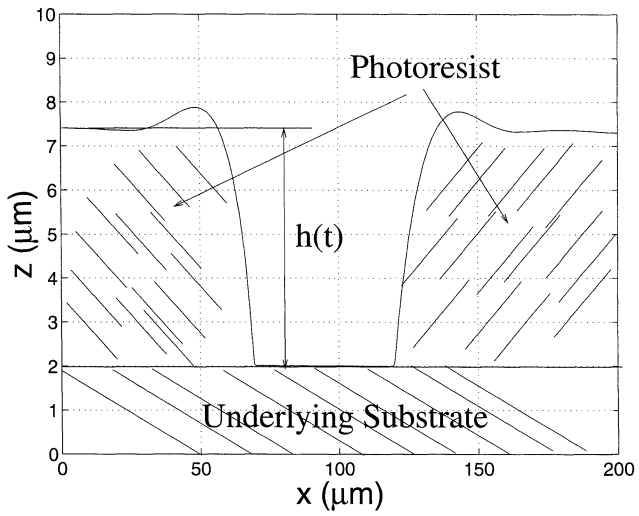

Figure 2. Definition of the dynamic trench height $h(t)$ for a typical photo-patterned trench with curved corners due to the post-baking.

are based on the physical properties of each material layer and are in general significantly different. This fact causes the photo-patterned trench height to vary with time. Repeated surface profiling during the milling process *in situ* monitoring of the trench height $h(t)$. Note that due to the scanning nature of the interferometer, the measurement of $h(t)$ will be discrete rather than continuous.

Figure 2 defines $h(t)$ for a typical photo-patterned trench. The curvature evident at the trench corners is due to post-baking of the photoresist. Photo-patterned parts are typically post-baked in the lithography process following exposure and development to drive residual solvent from the photoresist. It should be noted that for most applications $h(t)$ will decrease with time due to the fact that photoresist typically mills at a faster rate than most other materials of interest to the microelectronics industry.

Online state and parameter estimation

Extended Kalman Filter Formulation. It is necessary to incorporate the real-time measurement of trench height into the control system design to update model parameters online so as to correct for discrepancies between model predictions and the real-time state of the system. This is accomplished through the use of the discrete version of an extended Kalman filter parameter estimator, which is a well known computational algorithm for predicting optimal, nonbiased estimates of system parameters based on model predictions and process measurements (Ramirez, 1994).

The nonlinear formulation of the discrete Kalman filter is based on the following state and measurement equations

$$\boldsymbol{x}_{i+1} = \boldsymbol{f}_i(\boldsymbol{x}_i) + \boldsymbol{\Gamma}_1 \boldsymbol{w}_i \tag{9}$$

$$\varepsilon\{\boldsymbol{w}_i\} = \boldsymbol{0} \tag{10}$$

$$\mathrm{cov}\{\boldsymbol{w}_i\} = \boldsymbol{Q}_i \tag{11}$$

$$\boldsymbol{y}_i = \boldsymbol{h}_i(\boldsymbol{x}_i) + \boldsymbol{v}_i \tag{12}$$

$$\varepsilon\{\boldsymbol{v}_i\} = \boldsymbol{0} \tag{13}$$

$$\mathrm{cov}\{\boldsymbol{v}_i\} = \boldsymbol{R}_i \tag{14}$$

with initial conditions

$$\boldsymbol{x}(0) = \bar{\boldsymbol{x}}_0 + \boldsymbol{w}_0 \tag{15}$$

$$\varepsilon\{\boldsymbol{x}(0)\} = \bar{\boldsymbol{x}}_0 \tag{16}$$

$$\mathrm{cov}\{(\boldsymbol{x}(0) - \bar{\boldsymbol{x}}_0)\} = \boldsymbol{P}_0 \tag{17}$$

where $\boldsymbol{x}_i$ is the vector of state variables at step i, $\boldsymbol{y}_i$ is the measurement vector, $\varepsilon\{\boldsymbol{w}_i\}$ denotes the expected value of $\boldsymbol{w}_i$, $\mathrm{cov}\{\boldsymbol{w}_i\}$ denotes the covariance of $\boldsymbol{w}_i$, and $\boldsymbol{w}_i$ and $\boldsymbol{v}_i$ are the model uncertainty and measurement noise, respectively.

The state vector is defined to be the operating and material-specific parameters of the etch rate model

$$\boldsymbol{x} = \begin{bmatrix} J & V & \phi' & \boldsymbol{a}_s & \boldsymbol{a}_p & \boldsymbol{b}_s & \boldsymbol{b}_p \end{bmatrix}^T \tag{18}$$

$$\boldsymbol{a}_k = [a_{1,k} \quad a_{2,k} \quad a_{3,k} \quad a_{4,k}] \tag{19}$$

$$\boldsymbol{b}_k = [b_{1,k} \quad b_{2,k} \quad b_{3,k}] \tag{20}$$

where subscripts s and p denote the underlying substrate layer and the photoresist layer, respectively, for material-specific model parameters $\boldsymbol{a}$ and $\boldsymbol{b}$.

It is assumed that any dynamic behavior of the system states will be due solely to the effect of the modeling uncertainty $\boldsymbol{w}_i$. That is

$$\boldsymbol{f}_i(\boldsymbol{x}_i) = \boldsymbol{I} \tag{21}$$

$$\boldsymbol{\Gamma}_i = \boldsymbol{I} \tag{22}$$

In our application the single measurement of dynamic trench height h_i is a scalar. However, this measurement of trench height is directly proportional to the process time, thus precluding the reach of a steady-state measurement value. This causes the parameter estimator to become extremely aggressive after only a few (4 or 5) measurements, which is undesirable. This problem was circumvented by taking the measurement to be the difference in the etch rates of the substrate and photoresist layers

$$y_i(\boldsymbol{x}_i) = |c_s| - |c_p| \tag{23}$$

where c_s and c_p are the etch rates of the exposed portion of the underlying substrate layer and the photoresist, respectively. The absolute values of the material-specific etch rates c_k are required since etch rate is defined to be a negative velocity in the surface evolution model (Eq. 4), but in practice etch rates are taken to be positive.

Note that this differential etch rate can be inferred from the discrete interferometric measurements of trench height

as follows

$$y_i = \frac{(h_i - h_{i-1})}{\Delta t} \tag{24}$$

where Δt is the time between the discrete trench height measurements h_i.

Finally, the etch rates can be related to the model parameters through the combination of Eqs. 4, 5, 7 and 8. Thus

$$|c_k| = \frac{J}{N_k}\left(b_{1,k}V^2 + b_{2,k}V + b_{3,k}\right)\sum_{i=1}^{4} a_{i-1,k}\cos^{i+1}\phi' \tag{25}$$

Note that the angle of incidence between the incoming ion beam and the plane of the milling table ϕ' has been substituted for the more general spatially dependent beam angle ϕ in Eq. 25. The optimal estimate of ϕ' as determined by the Kalman filter is used to calculate the directional components of the incoming ion beam, which are then used to calculate the spatially dependent beam angle ϕ in the surface evolution model.

The formulation of the discrete version of the extended Kalman filter estimator continues with the definition of the following performance functional

$$J = \frac{1}{2}\left\{(\boldsymbol{x}-\boldsymbol{f})^T\boldsymbol{M}^{-1}(\boldsymbol{x}-\boldsymbol{f}) + (\boldsymbol{y}-\boldsymbol{h})^T\boldsymbol{R}^{-1}(\boldsymbol{y}-\boldsymbol{h})\right\} \tag{26}$$

where $\boldsymbol{M}$ is the covariance of the model uncertainty $\boldsymbol{w}$ and represents the uncertainty in the state prior to measurement.

The derivation of the Kalman filter proceeds with the minimization of the performance functional J with respect to the adaptive model parameters $\boldsymbol{x}$. The first term of Eq. 26 minimizes the model uncertainty $\boldsymbol{w}$, while the second term minimizes the measurement noise $\boldsymbol{v}$.

The following is the well-known solution to the discrete version of the extended Kalman filtering problem (Ramirez, 1994)

$$\hat{\boldsymbol{x}}_i = \bar{\boldsymbol{x}}_i + \boldsymbol{K}_i(\boldsymbol{y}_i - \boldsymbol{h}_i) \tag{27}$$

where

$$\bar{\boldsymbol{x}}_i = \boldsymbol{f}_i \tag{28}$$

$$\boldsymbol{K}_i = \boldsymbol{P}_i\left(\frac{\partial \boldsymbol{h}_i}{\partial \boldsymbol{x}_i}\right)^T \boldsymbol{R}^{-1} \tag{29}$$

$$\boldsymbol{P}_i = \boldsymbol{M}_i - \boldsymbol{M}_i\left(\frac{\partial \boldsymbol{h}_i}{\partial \boldsymbol{x}_i}\right)^T\left[\left(\frac{\partial \boldsymbol{h}_i}{\partial \boldsymbol{x}_i}\right)\boldsymbol{M}_i\left(\frac{\partial \boldsymbol{h}_i}{\partial \boldsymbol{x}_i}\right)^T + \boldsymbol{R}_i\right]^{-1}\left(\frac{\partial \boldsymbol{h}_i}{\partial \boldsymbol{x}_i}\right)\boldsymbol{M}_i \tag{30}$$

$$\boldsymbol{M}_{i+1} = \left(\frac{\partial \boldsymbol{f}_i}{\partial \boldsymbol{x}_i}\right)\boldsymbol{P}_i\left(\frac{\partial \boldsymbol{f}_i}{\partial \boldsymbol{x}_i}\right)^T + \Gamma_i\boldsymbol{Q}_i\Gamma_i^t \tag{31}$$

Here $\hat{\boldsymbol{x}}_i$ is the optimal estimate of the state vector. The covariance matrix $\boldsymbol{M}_i$ is the error of the estimate before the measurement, while the Riccati matrix $\boldsymbol{P}_i$ is the covariance of the error in the state estimate after measurement.

Kalman Filter Tuning. Tuning of the extended Kalman filter parameter estimator is accomplished through manipulation of the model uncertainty and measurement noise covariance matrices $\boldsymbol{Q}$ and $\boldsymbol{R}$ of Eqs. 11 and 14, respectively. For simulation purposes, the noise level in the trench height measurement is assumed to be 1% so that

$$R = 0.01^2 \tag{32}$$

in each of the three case studies.

During tuning of the model covariance matrix $\boldsymbol{Q}$, it becomes apparent that, for ideal system performance, it is necessary to tune the system based on the anticipated type of process fault. That is, the estimation system exhibits the best performance when different sets of tuning parameters are employed in the presence of system-wide and material-specific process faults. The final determination of which set of tuning parameters to employ will ultimately be made in the field based on the history of past process faults and operator experience.

When system-wide process faults are present, the following set of tuning parameters is found to produce an acceptable system response when the full state vector ($\boldsymbol{x}_1$) is implemented

$$\boldsymbol{x}_1 = \begin{bmatrix} J & V & \phi' & \boldsymbol{a}_s & \boldsymbol{a}_p & \boldsymbol{b}_s & \boldsymbol{b}_p \end{bmatrix} \tag{33}$$

$$\boldsymbol{Q} = \mathrm{diag}[0.5^2 \quad 0.1^2 \quad 0.01^2 \quad \mathbf{0.01^2} \quad \mathbf{0.02^2} \quad \mathbf{0.01^2} \quad \mathbf{0.02^2}] \tag{34}$$

The diag notation indicates that the actual $\boldsymbol{Q}$ matrix contains the values listed in brackets along the principal diagonal and zeros in the remaining matrix elements.

It is important to remember the significance of the matrix $\boldsymbol{Q}$, which is the covariance of the model uncertainty. The values along the principal diagonal of $\boldsymbol{Q}$ represent the variances of the individual states and parameters which comprise the state vector. High variances are indicative of high levels of uncertainty, and the Kalman filter formulation is such that the Kalman gain for states with high levels of uncertainty is higher than for those states with lower variances. This results in larger changes in the magnitude of these states during the estimation process.

Examination of Eq. 34 shows that the Kalman gain associated with this tuning scenario will be highest for the state variables J and V and lowest for the state variable ϕ' and the material-specific parameters ($\boldsymbol{a}_s$, $\boldsymbol{a}_p$, $\boldsymbol{b}_s$, and $\boldsymbol{b}_p$). The high variances associated with the ion beam current density and voltage (J and V) allow the state vector to respond quickly to the presence of system-wide process faults which affect the etch rates of both material layers. The variance of the table angle ϕ' is relatively low since there is little uncertainty associated with this process state, and higher levels of the variance result in estimations of the table angle which are physically unrealistic. The non-zero variances of the material-specific parameters allow for the adaptation of the individual material etch rates for cases in which both system-wide faults

and material-specific faults are present. Increasing the variances of the material-specific parameters has no significant effect on the final filter predictions, but causes an increase in the response time of the system, which is undesirable.

Finally, note that the variances of parameters associated with the photoresist layer are twice those associated with the substrate layer. During the experimentation performed to determine initial values of the material-specific parameters $\boldsymbol{a}$ and $\boldsymbol{b}$, it was observed that the uncertainty of the photoresist parameters are approximately twice that of the substrate materials investigated (Klein and Ramirez, 2000). This is due to the fact that the photoresist is a polymer material and its properties can change drastically in the high temperature of the ion milling environment.

The following set of tuning parameters produces an acceptable system response in the presence of material-specific process faults

$$\boldsymbol{Q} = \mathrm{diag}[0.1^2 \quad 0.1^2 \quad 0.01^2 \quad \mathbf{0.02^2} \quad \mathbf{0.04^2} \quad \mathbf{0.02^2} \quad \mathbf{0.04^2}] \tag{35}$$

Notice that in this case the variance of the ion beam current density J has been reduced and the variances of the material-specific parameters have been increased. This allows the etch rates of the individual layers to adapt to the material-specific process fault, while the operating states which affect both material layers remain relatively constant.

Kalman Filter State-Space Reduction. The state vector of Eq. 18 contains 17 operating and material-specific parameters. In addition to resulting in an excessive computational burden, this large state vector of adaptive parameters significantly complicates the tuning of the filter due to the different time scales associated with each class of adaptive parameters.

These problems can be overcome by reducing the size of the state vector. Examination of Eq. 18 shows that the state vector is comprised of three operating parameters (J, V, and ϕ') and seven model parameters specific to each of the two material layers ($\boldsymbol{a}_s$, $\boldsymbol{a}_p$, $\boldsymbol{b}_s$, and $\boldsymbol{b}_p$) for a total of 17 adaptive parameters. It is essential that the state vector be comprised of both operating parameters and material-specific model parameters so that the control system can account for both system-wide and material-specific process faults. However, the fact that there are 14 material-specific parameters and only three operating parameters present in the state vector suggests that the number of material-specific parameters can be significantly decreased.

Table 1. Initial Estimates of Al_2O_3 Model Parameters

	Alumina		Photoresist	
i	a_i	b_i	a_i	b_i
1	1.18×10^1	-3.46×10^{-6}	3.22×10^2	-2.77×10^{-6}
2	-3.83×10^1	5.66×10^{-3}	-9.03×10^2	4.56×10^{-3}
3	4.38×10^1	-1.15	8.88×10^2	-7.37×10^{-1}
4	-1.73×10^1	N/A	-3.00×10^2	N/A

From Klein and Ramirez (2000).

The partial removal of the material-specific etch rate parameters from the state vector suggests that no error is associated with these removed parameters and that any discrepancy between the actual etch rate of the material and the model predicted etch rate is due to the parameters remaining in the state vector. This of course is incorrect. However, it is shown that the removal of carefully selected subsets of material-specific parameters from the state vector results in a significant decrease in computational time and does not adversely affect the overall performance of the Kalman estimator.

Case studies based on three separate state vectors were performed. The extent of reduced computational time and the associated degradation in filter performance for systems based on each of the three following state vectors are compared

$$\boldsymbol{x}_1 = \begin{bmatrix} J & V & \phi' & \boldsymbol{a}_s & \boldsymbol{a}_p & \boldsymbol{b}_s & \boldsymbol{b}_p \end{bmatrix}^T \tag{36}$$

$$\boldsymbol{x}_2 = \begin{bmatrix} J & V & \phi' & \boldsymbol{a}_s & \boldsymbol{a}_p \end{bmatrix}^T \tag{37}$$

$$\boldsymbol{x}_3 = \begin{bmatrix} J & V & \phi' & \boldsymbol{b}_s & \boldsymbol{b}_p \end{bmatrix}^T \tag{38}$$

where $\boldsymbol{x}_1$ represents the complete state space, and $\boldsymbol{x}_2$ and $\boldsymbol{x}_3$ are reduced state vectors based on material-specific parameters $\boldsymbol{a}$ and $\boldsymbol{b}$, respectively. Note that $\boldsymbol{b}$ and $\boldsymbol{a}$ are held constant at their nominal values during the implementation of state vectors $\boldsymbol{x}_2$ and $\boldsymbol{x}_3$, respectively.

For the purpose of this set of simulations, it is assumed that an interferometric measurement of trench height is performed once every minute so that the simulated differential etch rate measurement y_i of Eq. 23 is updated every 60 s in the stimulations (that is, $\Delta t = 60$). In practice, the actual sampling period will need to be developed based on the process at hand. Obviously, a greater sampling frequency will

Table 2. Results of Kalman Filter Case Studies

Case Study	State Vector	Layers Containing Error	Flops	Response Time (Δt)	Offset in Photoresist Etch Rate		Offset in Al_2O_3 Etch Rate	
					+20% Error	−20% Error	+20% Error	−20% Error
1	$\boldsymbol{x}_1$	Both	73.2×10^3	3	−33.2%	−28.9%	−47.9%	−41.8%
2	$\boldsymbol{x}_1$	Photo Only	73.2×10^3	3	4.7%	−14.3%	N/A	N/A
3	$\boldsymbol{x}_2$	Both	25.8×10^3	4	−29.7%	−25.5%	−42.8%	−36.6%
4	$\boldsymbol{x}_2$	Photo Only	25.1×10^3	4	5.7%	−11.1%	N/A	N/A
5	$\boldsymbol{x}_3$	Both	15.9×10^3	2	−10.6%	−7.8%	−15.7%	−11.5%
6	$\boldsymbol{x}_3$	Photo Only	15.9×10^3	4	1.6%	−4.4%	N/A	N/A

lead to better control of etch depth. The sampling frequency should be significantly increased for shorter processes to provide the etch depth controller with a sufficient amount of feedback data. However, note that in practice the interferometric measurement will be performed through an optically-pure, shuttered view port in the ion milling chamber. This view port is susceptible to the buildup of sputtered materials when it is exposed to the ion milling environment. Exposure of the view port to the milling environment must be minimized to prolong the workable life of the view port. Thus, there is a tradeoff between the number of data points collected and the maintenance cost due to the replacement of the view port which must be evaluated in the field to determine an acceptable measurement frequency for the control system.

In each of the case studies, the underlying substrate material is specified to be a 2 μm layer of alumina (Al_2O_3) and the initial photoresist height is set to 6 μm. Nominal values of the operating states J, V, and ϕ' are set at 0.57 mA/cm^2, 600 eV and 60°, respectively, which are the conditions at which the model parameters were determined (Klein and Ramirez, 2000). The final time of the simulations is 20 min. Initial estimates of $\boldsymbol{a}$ and $\boldsymbol{b}$ have been previously determined experimentally for alumina and photoresist (Klein and Ramirez, 2000) and are listed in Table 1.

The results of the case studies are presented in Table 2. Column 4 of Table 2 contains the number of flops, or floating point operations, performed during the simulations. The response times reported in column 5 are the number of measurement periods required for the predicted etch rates to rise to 95% of the actual etch rates in both material layers. The offset between the final predicted etch rates and the actual etch rates is shown as the scaled percentage of the difference between the estimated and actual etch rates of the case study. This statistic is not available for the alumina etch rate in the case studies where error is introduced in the photoresist layer only because the expected change in alumina etch rate is zero. However, the actual change in alumina etch rates for these case studies was negligible, on the order of 0.005 nm/s.

It can be seen by examining Table 2 that computational burden is the lowest when state vector $\boldsymbol{x}_3$ is implemented. In fact, computational burden is reduced by 80% when reduced state vector $\boldsymbol{x}_3$ is substituted for the full state vector $\boldsymbol{x}_1$. In addition, the response times and prediction offsets show superior performance when state vector $\boldsymbol{x}_3$ is implemented. Finally, state vector $\boldsymbol{x}_3$ is the preferred state vector from a physical standpoint as well, since the material-specific $\boldsymbol{b}$ parameters describe the functionality of the yield function with respect to beam voltage while the $\boldsymbol{a}$ parameters describe the functionality of the yield function with respect to table angle. Beam voltage, being a function of the state of the ion beam, exhibits relatively large variability when compared to that of the milling table angle, which is a mechanical system parameter and does not exhibit significant within-run variation due to the physical design of the milling system. State vector $\boldsymbol{x}_3$ is therefore chosen as the superior of the three state vectors investigated and is the state vector implemented in the on-line proof of concept experiments (as will be discussed later). The poor performances of $\boldsymbol{x}_1$ and $\boldsymbol{x}_2$ are due to the slow dynamics and highly nonlinear functionality of the material-specific $\boldsymbol{a}$ parameters in the etch rate model.

Experimental Method

The heterodyne laser interferometer was installed on an ion milling apparatus so that the online performance of the etch depth controller could be investigated. The laser interferometer is comprised of an HP5517A laser head and an HP53132A frequency counter (Hewlett Packard, Santa Clara, CA), as well as various optical components including several mirrors and lenses (Edmund Industrial Optics, Barrington, NJ) and polarizing wave plates (Meadowlark Optics, Frederick, CO).

Figure 3 contains a depiction of the common-path measurement and reference arms of the interferometer. Note that the laser beam must be perpendicular to the target to allow monitoring of the reflected phase. A vacuum chamber was designed with an optically pure view port angled at 0.52 rad (30°) to facilitate measurements at a table angle of 1.05 rad (60°). A detailed description of the interferometric device can be found elsewhere (Klein et al., 2000; Klein, 2000).

The ion milling apparatus consists of a 6 in. (152 mm) ion gun and an IT-3500 Ion Source Controller (Ion Tech, Fort Collins, CO), as well as a CHA vacuum control system (CHA Industries, Menlo Park, CA) with a cryogenic high-vac pump (CTI-cryogenics, Mansfield, MA). Milling is performed using an Ar^+ ion beam. The milling table itself is a pre-existing in-house design (StorageTek, Louisville, CO), which is water-cooled and allows for the tilting and rotating of the table in the azimuth plane during milling.

The wafers investigated are comprised of a 2 μm layer of titanium evaporated onto ferrite substrates using a CHA Industries Mark 40 evaporation system (CHA Industries, Menlo Park, CA) and subsequently patterned with a photoresist layer. The photo-lithography process consists of coating the wafer with AZ P4400 photoresist (Hoechst-Celanese, Somerville, NJ) in a SVG-8126PC/8136HPO spin coater (Silicon Valley Group, Inc., San Jose, CA) operated at 2,000 rpm. The wafers are then soft baked at 90°C for 30 min before exposure in a Perkin Elmer 310HT mask aligner system (Perkin Elmer, Norwalk, CT). Exposed resist is developed using AZ400K photoresist developing solution (Hoechst-Celanese, Somerville, NJ) and is then post-baked at 125°C for 45 min to drive off excess solvent and harden the photomask before ion milling.

Online Fault Detection

Since the completion of the model development experiments reported elsewhere (Klein and Ramirez, 2000), a major change has occurred in the performance of the ion gun of the experimental equipment. We were no longer able to reach the beam conditions employed in the identification experiments. The ion controller had malfunctioned and was sent out for repair. After this repair, the ion gun still could not perform up to specifications. Either the ion controller output is malfunctioning or the permanent magnets in the ion gun have degraded to the point of not being able to provide a plasma similar to that of the original experiments.

The maximum attainable current density is now approximately 0.35 mA/cm^2 as opposed to the 0.57 mA/cm^2 at which the model development experiments were performed. The significant decrease in beam current density results in a large

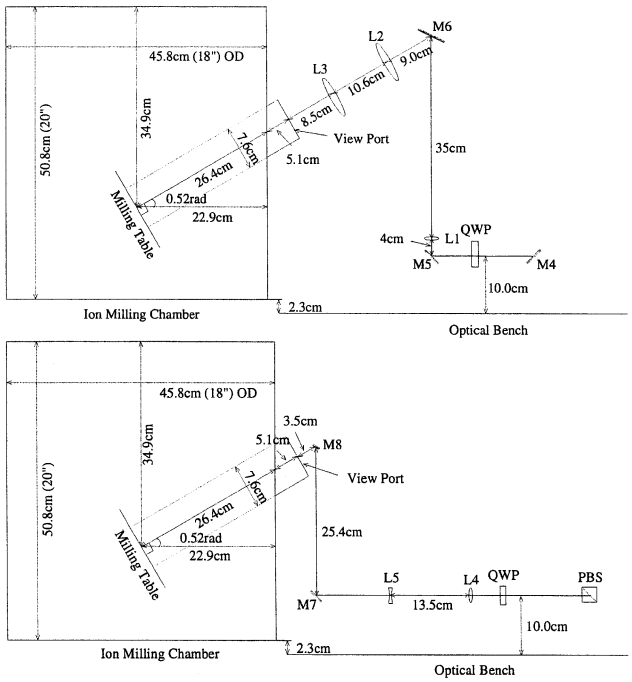

Figure 3. Side-view of measurement arm (top) and reference arm (bottom) of the interferometer.

M4, M5 = 2.54 cm mirrors; M6 = 7.5 cm mirror; M7 = 2.54 cm mirror; M8 = 1.5 cm × 0.5 cm mirror; L1 = 2.54 cm × 4 cm lens; L2, L3 = 7.5 cm × 40 cm lens; L4 = 2.54 cm × 22.5 cm lens; L5 = 2.5 cm × − 10 cm lens; QWP = quarter-wave plate; PBS = polarizing beam splitter (complete description of the measurement system design can be found elsewhere (Klein et al., 2000; Klein, 2000)).

uncertainty in the etch rate model due to the lack of experimental data at this reduced current density. The remainder of the operating parameters were kept identical to those of the identification experiments (that is, 600 eV beam voltage and a table angle of 1.05 rad (60°)).

The pre-existing design of the ion milling table did not possess the stability required for precise interferometric measurements. This led to an excessive amount of milling table vibration attributed to the pump stroke of the cryogenic high-vac pump (CTI-Cryogenics, Mansfield, MA). While the common-path design of the interferometer was able to attenuate this noise (without the common-path design, the phase signal was observed to be indistinguishable from the background noise), it was not able to overcome the excessive amounts of noise present in the system. It was therefore necessary to shut down the pumping system while performing the interferometric trench height measurements.

While this milling system, which had been designed as an inexpensive research and development tool, did not allow the interferometer to be tested in a true manufacturing environment, it was adequate for the proof of concept demonstration detailed in this article. The purpose of this work was to demonstrate the usefulness of the online fault detection system, and the shortcomings of the particular experimental apparatus available for this work should not detract from the implications of the final results reported in this article. Ion milling systems typically employed in manufacturing environments possess greater table stability than that of the research tool available to the authors during this investigation.

Since the table angle was set at 1.05 rad, it was not necessary to adjust the table angle to perform the measurements since the incoming angle of the ion beam is 0.52 rad (30°). In addition, due to the lack of precision in the control of table rotation, the milling table was not rotated during these online proof of concept experiments. This allowed us to avoid having to re-focus the interferometer (which is not a trivial task) prior to each measurement. To alleviate shadowing of the trench floor in the absence of table rotation, a wafer feature in the plane perpendicular to the ion beam was chosen for study.

Online identification of model parameters with a large change in ion gun performance

The first case study consisted of monitoring the etching of a 2 μm titanium film patterned with a 6 μm layer of photoresist. Titanium was chosen as the material for this case study due to the fact that it possesses a larger difference in the photoresist to substrate etch rate. This leads to a relatively high differential etch rate and a faster change in the height of the photo-patterned trench, leading to a relatively large signal-to-noise ratio in the measurement system.

Initial Profiling. The trench monitored in this case study was measured with a Tencor (Alpha-Step, KLA Tencor, San Jose, CA) stylus-based profiling device prior to the experiment to verify the accuracy of the interferometric measurements. Figure 4 contains the initial profile as measured with the Tencor device. The trench height was determined to be 5,970 ± 45 nm, while the width was measured to be 130 ± 2 μm.

The wafer was then fixed to the milling table and the interferometer was focused through the vacuum chamber onto the same photo-patterned feature which was measured with the Tencor device. Five scans were performed in order to obtain an estimate of the error in the interferometer measurement system, which was needed to properly tune the Kalman filter parameter estimator. It was possible to profile only half of the trench investigated in this study due to the large trench width and the fact that the signal-to-noise ratio of the interferometer decreases rapidly with scan length due to the quadratic dependence of the phase base line on scanner posi-

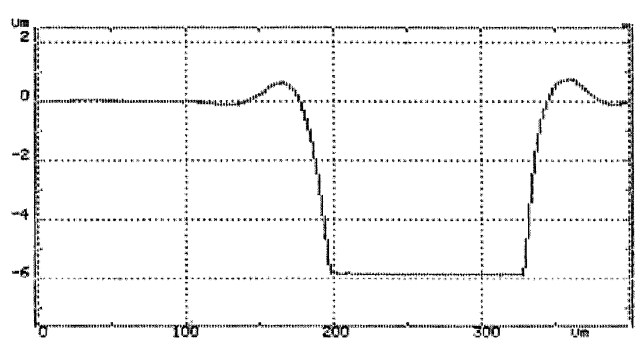

Figure 4. Tencor scan of initial profile for case study No. 1, trench height = 5,970 ± 45 nm.

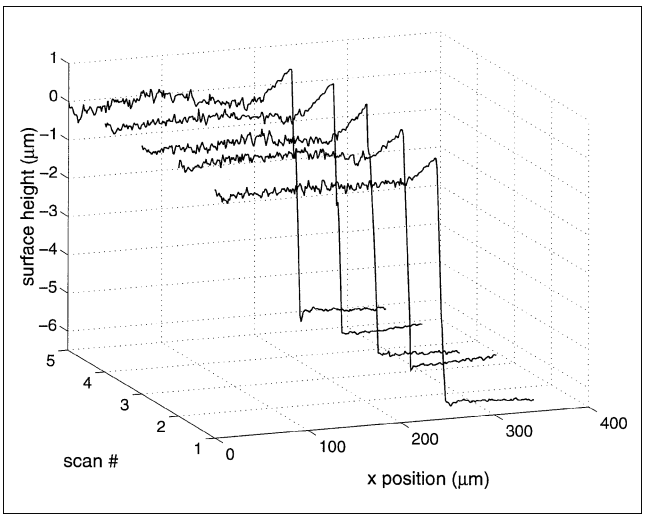

Figure 5. Initial surface profiles for case study No. 1 using online implementation of the interferometric measurement system, trench height = 5,856 ± 73 nm.

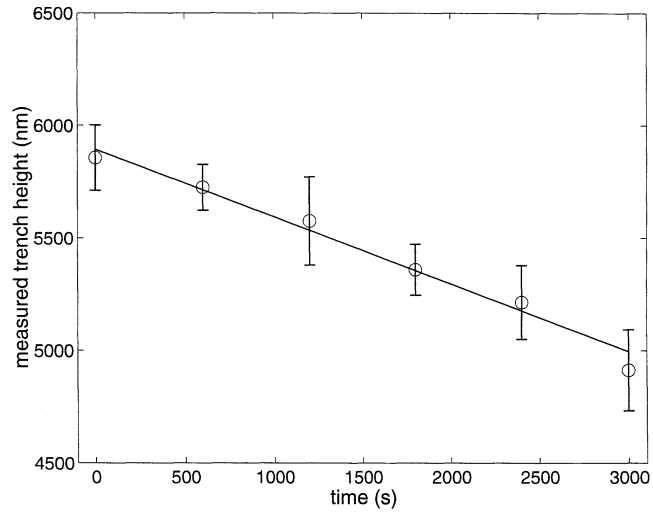

Figure 6. Case study No. 1 trench height measurements with two standard deviation error bars and linear trend line ($R^2 = 0.99$).

tion (Klein, 2000). Figure 5 contains the 5 initial profiles obtained using the interferometer. Examination of Figure 5 shows that the measurements are highly repeatable, although the level of noise is higher than desired due to the pre-existing design of the milling table which does not possess the stability required for precision interferometric measurements. The initial trench height was determined to be 5,856 $\pm$73 nm by the interferometer, which corresponds well with that measured using the Tencor profiler, 5,970$\pm$45 nm.

Although 73 nm of noise does not appear to be large compared to the 5,856 nm measurement at first glance, we are using an *a priori* estimate of the integer fringe number in analysis of the phase data (Klein et al., 2000). Therefore, the 73 nm of noise actually needs to be compared with our signal bandwidth of 2π rad (360°). The standard deviation then becomes 73 nm out of 316 nm (0.23), so that the variance of the measurement is set at $R = 0.05$ in the Kalman filter parameter estimator.

Obviously, this noise level is higher than is desirable and effectively renders the measurement system to be a gross trend detection system only. However, this noise level, which is an order of magnitude higher than that exhibited in the laboratory setting (Klein et al., 2000), is expected to be much less when the interferometer is employed on a state-of-the-art milling system which possesses better table stability. In spite of the large measurement noise levels exhibited by this implementation of the measurement system, we are still able to accurately track the state of the physical system through the use of the Kalman filter.

Results and Analysis. Due to the error in the ion gun, the nominal beam current density of this experiment (0.35 mA/cm^2) is significantly different from that of the model identification experiments (0.57 mA/cm^2) so that we are operating in a regime in which our etch rate model has not been validated experimentally and therefore possesses a higher level of uncertainty. Furthermore, although the beam current density is measured directly through the use of a Faraday cup, we are not confident that the plasma generated by the system in the presence of the ion gun process fault is equivalent to that used in the model identification experiments. Under these adverse systemic conditions, the photoresist exhibits an etch rate which is roughly 50% of that predicted by the model whereas the titanium exhibits an etch rate which is approximately 20% of the model predicted value (Klein, 2000). Although the ion gun error is obviously undesirable, the situation at hand actually lent itself to the proof of concept experiments for the online-fault detection system as is shown below.

The variance of beam density, as well as those of the titanium parameters, were increased so as to allow the Kalman parameter estimator to adapt to the large uncertainties in these parameters. The following tunings were found to result in model predictions which accurately track the state of the physical system in the presence of this large error

$$R = 0.05 \tag{39}$$

$$Q = \mathrm{diag}[0.7^2\ 0.09^2\ 0.01^2\ 0.4^2\ 0.4^2\ 0.4^2\ 0.1^2\ 0.1^2\ 0.1^2] \tag{40}$$

Milling was performed for a total of one hour, with the process being stopped and the cryogenic pump turned off to allow for scanning with the measurement system after every 10 min of milling. The measured trench heights are reported with two standard deviation error bars in Figure 6. Note the linear trend with an R^2 value of 0.99. This shows that trench height decreases linearly with time, which suggests that the differential etch rate remains constant throughout the experiment.

Figure 7 contains the estimated etch rates. Note that, with these tunings, the correction on the titanium etch rate is far more aggressive than is that on the photoresist etch rate. This is due to the tunings of the Kalman filter, and is in fact desirable in the presence of the large model identification uncer-

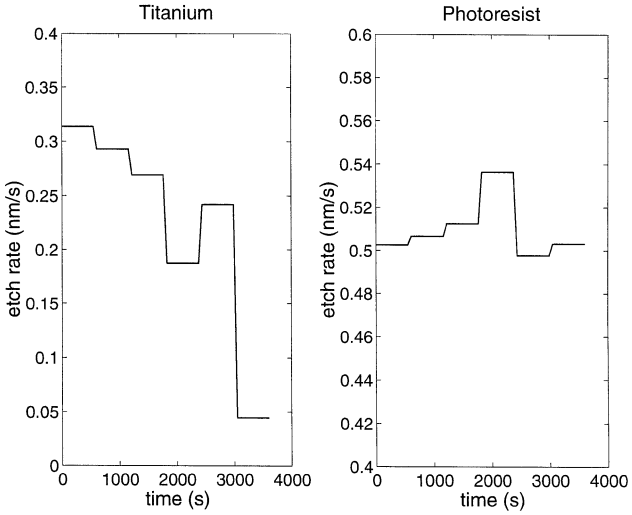

Figure 7. Etch rate response of the online measurement and estimation system for case study No. 1.

tainty. That is, it is assumed that we are more interested in controlling the etch rate of the titanium layer than that of the photoresist layer, which results in the new parameter estimation weights listed above. While errors in the estimation of the photoresist etch rate will lead to errors in the prediction of shadowing effects on the trench floor, this is not as crucial to determining proper stopping times for the process as are errors in the predicted etch rate of the titanium layer.

The predicted stopping times after each measurement are shown in Figure 8. The final predicted stopping time of 193.4 min should yield a final etch depth of $z = -696$ nm based on the nominal experimental titanium etch rate of 0.06 nm/s. This value is significantly closer to the original target of $z = -1{,}166$ nm (model predicted depth after 60 min of milling) than was the actual experimental etch depth of $z = -222$ nm

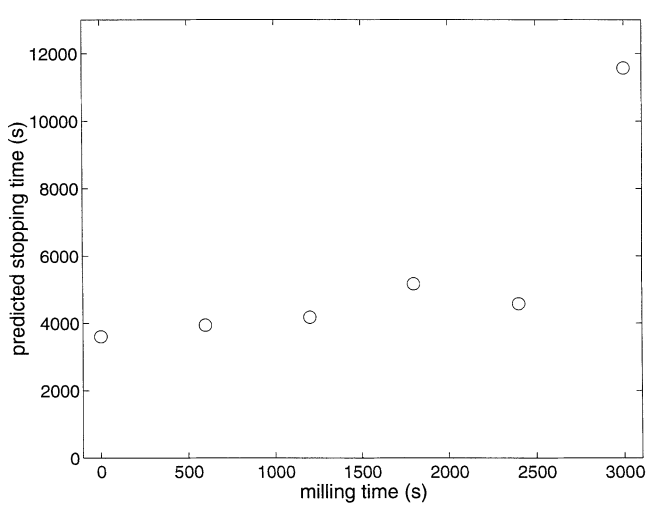

Figure 8. Predicted stopping times required to reach the etch depth target of $z = -1{,}166$ nm of case study No. 1.

after only 60 min of milling time. This shows that the properly tuned control system is capable of attenuating the negative effects of even large model discrepancies and process faults.

The large difference between the actual and targeted etch depths in this case study is due largely to the slow measurement frequency employed. Obviously, the sooner the first measurement is performed in the run, the sooner the presence of a process fault can be detected and the stopping time adjusted accordingly. The Kalman estimator keeps the values of the parameters at their nominal levels prior to the first measurement, so that in this case the model is run for 10 min before the etch rates are changed to adapt to the physical state of the experimental system. Furthermore, examination of Figure 7 shows that several (4 or 5) measurements are required before the parameter estimation system is able to closely track the actual process conditions. These trends indicate that it is important to perform as many measurements as are practically feasible early in the process run so that the process faults are identified in a timely manner and the estimation system can predict a reasonable stopping time, thereby closely controlling the final etch depth to acceptable levels. The extended Kalman filter has been shown to function well in other fault detection and diagnosis situations (Korbicz et al., 1993).

Monitoring Using Prior-Run Identified Model Parameters. The operating conditions of run No. 2 are identical to those of the prior run (run No. 1), namely a beam density of 0.35 mA/cm^2, a beam voltage of 600 eV, and a table angle of 1.05 rad. The target depth was set at $z = -225$ nm so as to limit the final milling to approximately 1 h based on the etch rates exhibited in run No. 1.

The initial model parameters were taken to be those determined by the Kalman filter estimation system in run No. 1 in the presence of the process fault as shown in Table 3. Note that the beam current density (J) and the titanium parameters ($b_{i,s}$) exhibit the largest change from their nominal values. This is due to the large uncertainty and the relatively high filter gain for these parameters as has been described in the previous subsection. Using these new model parameters, we are able to relax the tunings of the Kalman filter back to less aggressive values

$$R = .05 \tag{41}$$

$$\boldsymbol{Q} = \mathrm{diag}[.09^2 .09^2 .01^2 .09^2 .09^2 .09^2 .2^2 .2^2 .2^2] \tag{42}$$

Table 3. Nominal and Estimated Values of the Model Parameters in the Presence of the Process Fault

Parameter	Nom. Value	Est. Value	% Diff.
J	0.35 mA/cm^2	0.34 mA/cm^2	−2.9%
V	600.0 eV	599.3 eV	−0.1%
ϕ'	1.047 rad	1.047 rad	0.0%
$b_{1,p}$	-2.77×10^{-6}	-2.76×10^{-6}	0.3%
$b_{2,p}$	4.56×10^{-3}	4.59×10^{-3}	0.9%
$b_{3,p}$	-7.37×10^{-1}	-7.34×10^{-1}	−0.4%
$b_{1,s}$	-4.12×10^{-6}	-4.29×10^{-6}	−4.6%
$b_{2,s}$	6.82×10^{-3}	5.85×10^{-3}	−14.0%
$b_{3,s}$	−1.61	−1.82	−12.5%

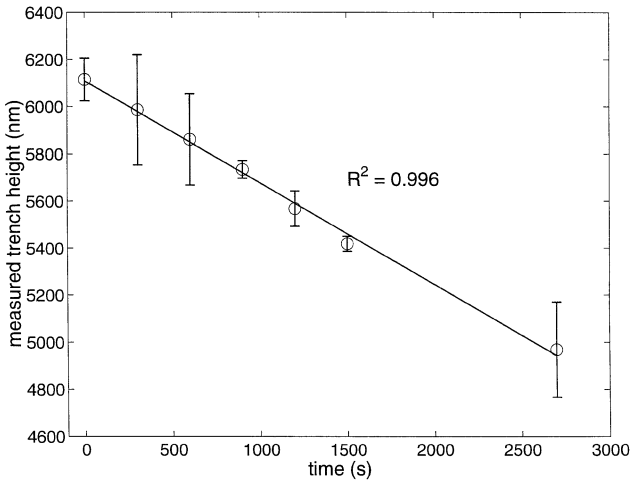

Figure 9. Case study No. 2 trench height measurements with two standard deviation error bars and linear trend line ($R^2 = 0.996$).

These tunings have a fundamental basis since the model identification experiments for the titanium and photoresist materials exhibited standard deviations of 0.09 and 0.20, respectively (Klein and Ramirez, 2000). The variances of the operating parameters J and V were assumed to be equal to those of the titanium model parameters. The variance was set at the relatively low value of 0.01^2 for the table angle ϕ' since this parameter is known with a high degree of certainty.

This experiment demonstrates both the repeatability and the tracking ability of the control system using a new set of model parameters identified in run No. 1, the use of which significantly decreases model uncertainty in the presence of the process fault.

Results and Analysis. As has been stressed previously, the performance of the controller is directly related to how frequently measurements are performed and at what time the first measurement is taken. It is important that the first measurement be taken early on in the process so as to allow for correction of the model predictions before a significantly long time has elapsed. Obviously, the sooner a process disturbance is detected, the sooner the predicted stopping time can be adjusted to account for this disturbance, leading to higher accuracy in the etch depth controller. Also, as shown earlier, the controller requires several (4 or 5) measurements before the etch rates of the individual material layers approach their actual values in the presence of large process disturbances. After supplying the controller with a sufficient amount of data early on in the run, it is then possible to decrease the measurement frequency for the remainder of the run. For these reasons, measurements were performed every 5 min for the first 25 min and every 20 min for the remainder of run No. 2, in contrast to the 10 min measurement period employed in run No. 1.

The measured trench heights with two standard deviation error bars are reported in Figure 9. Notice that the height measurements again decrease linearly with time ($R^2 = 0.996$) indicating that the differential etch rate is constant throughout the experiment.

Again, the Kalman filter was used to make optimal estimates of parameter values based on the measurements presented in Figure 9. The surface evolution model was used to predict the stopping time required to reach the target depth of $z = -225$ nm using the estimated values of the model parameters. The values of this predicted stopping time after each measurement are shown in Figure 10. Notice again that it takes several measurements for the stopping time to be adjusted to its final value, which in this case study was determined to be 56.4 min.

To further illustrate the response of the optimal parameter estimation system, consider Figure 11, which depicts the estimated values of the individual material etch rates. Notice that while the etch rates of both materials are adjusted, the etch rate of the photoresist is adjusted much more than is that of

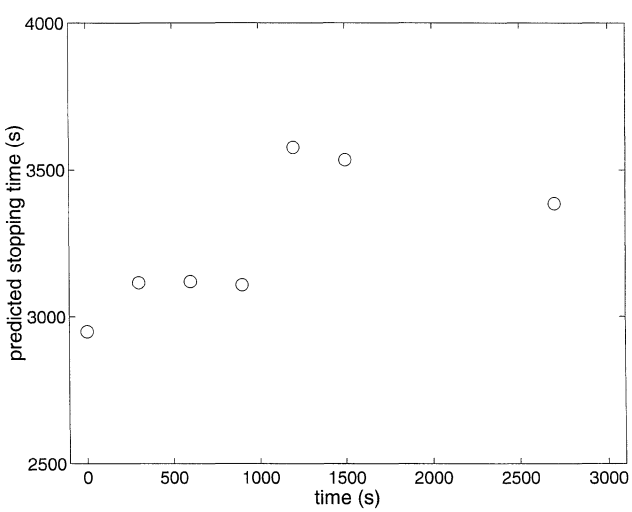

Figure 10. Predicted stopping times required to reach the etch depth target of $z = -225$ nm of case study No. 2.

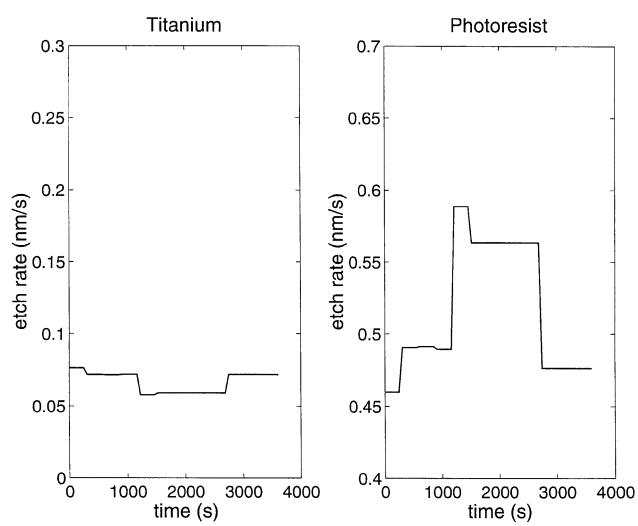

Figure 11. Etch rate response of the online measurement and estimation system for case study No. 2.

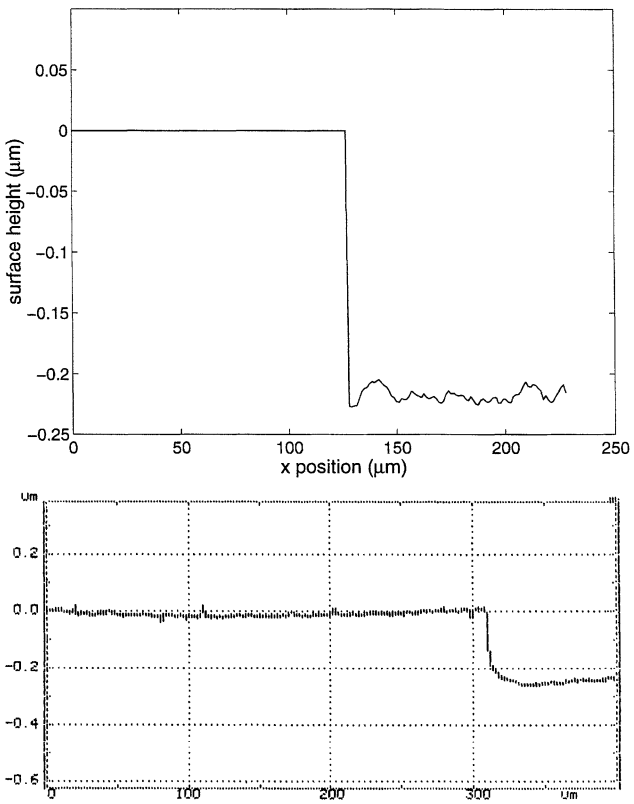

Figure 12. Final predicted (top) and measured (bottom) etch depth into the titanium layer for case study No. 2.

the titanium based on the tunings employed in this case study. This is due to the fact that since we are employing the new model parameters determined in case study No. 1, the majority of the modeling uncertainty is once again in the photoresist layer due to the uncertainty of the original identification experiments (Klein and Ramirez, 2000). Although this causes an offset in the estimated and actual photoresist etch rates (since the actual etch rate is less than the nominal etch rate, not slightly greater as is predicted by the estimation system), which could lead to small variations in the surface evolution model predictions of the trench floor due to shadowing calculations based on the ensuing incorrect photoresist height, the main goal is to control the etch depth in the titanium layer. Due to the fact that the photoresist and titanium etch rates are of opposite signs in the measurement equation (Eq. 23), it was difficult to determine filter tunings which were capable of adjusting both the etch rate of the photoresist layer and that of the titanium layer to their experimental values in the presence of the extraordinarily large process fault.

Finally, consider Figure 12, which contains the predicted final profile and a Tencor scan of the final etch profile into the titanium layer. The final etch depth as measured by the Tencor scanner was determined to be $z = -250 \pm 37$ nm. This corresponds extremely well with the targeted etch depth of $z = -225$ nm. Thus, it is shown that the parameters estimated in run No. 1 significantly improve the uncertainty of the model predictions, thus allowing the control system to accurately track the state of the physical process in the presence of the large process fault.

Based on Tencor scans of the final surface profile prior to and after removal of the photoresist layer, the actual values of the photoresist and titanium etch rates were determined to be 0.31 ± 0.1 nm/s and 0.07 ± 0.02 nm/s, respectively. Referring back to Figure 11, it can be seen that the predicted titanium etch rate closely matches that of the actual etch rate present in the system. The predicted photoresist etch rate, however, does not match its experimental value as closely as that of the titanium. As explained previously, this is due to the tunings employed in the model identification experiment of run No. 1 which are required to correctly predict the titanium etch rate in the presence of the process fault, which is the main goal of the online controller.

The small shadowing effect present in the trench floor in the measured profile of Figure 12 is due both to the relative inaccuracy of the Tencor device in measuring small (that is, ≈ 100 nm) changes in surface height and to the fact that the wafer was not rotated during milling. The model does not predict this extent of shadowing since for modeling purposes the feature was taken to be perpendicular to the ion beam during milling, while in practice this exact alignment is impossible to achieve and any offset in this alignment will lead to minor shadowing effects in the finished part. This will not be an issue in practice since the wafer will be rotated during milling. Again, rotation was absent during these proof of concept experiments to alleviate the burden of having to re-focus the interferometer prior to each measurement, with the loss of focus attributed to the poor table stability of the ion milling system used in this work.

Conclusions

The design of an automatic control system for etch depth in an ion milling process is presented. The control system is based on 3-D model predictions of surface profile evolution and ion milling etch rates. The use of a heterodyne laser interferometer is proposed for obtaining *in situ* measurements of the dynamic trench height during the milling process. Model parameters are adapted on-line through the use of an extended Kalman filter and the interferometric measurement of the dynamic trench height, facilitating accurate model predictions and the control of final etch depth. The control policy is inherently bang-bang as the only available control action is the on/off state of the ion beam.

The design and tuning of an extended Kalman filter is described in detail. Computational burden associated with the implementation of the extended Kalman filter is reduced through the use of a simplified state space description of the system. It is shown that the adaptive parameter estimation scheme presented in this work is capable of attenuating the effects of this model mismatch and of accurately predicting stopping times in the presence of this large modeling uncertainty. It should be noted that although the experimental work in this article was performed on patterned features of the size commonly found in the tape drive industry (that is, ≈ 100 μm), the methodology can be easily extended to more advanced technologies through the inclusion of an appropriately sized measurement spot on the patterned wafers.

Acknowledgments

This research was funded by StorageTek (Louisville, CO). The authors would like to thank Dr. John Hall of JILA and NIST, Boulder, CO, for his assistance in the design and implementation of the heterodyne interferometer.

Literature Cited

Arnold, J., H. Sawin, M. Dalvie, and S. Hamaguchi, "Simulation of Surface Topography Evolution During Plasma Etching by the Method of Characteristics," *J. of Vacuum Sci. and Technol. A*, **12**, 620 (1994).

Beall, J., M. Cromar, T. Harvey, M. Johansson, R. Ono, C. Reintsema, D. Rudman, S. Asher, A. Nelson, and A. Swartzlander, "$YBa_2Cu_3O_{7-\delta}$/Insulator Multi-Layers for Crossover Fabrication," *IEEE Trans. on Magnetics*, **27**, 1596 (1991).

Benson, T., L. Kamlet, S. Ruegsegger, C. Hanish, P. Hanish, B. Rashap, P. Klimecky, J. Freudenberg, J. Grizzle, P. Khargonekar, and F. J. Terry, "Sensor Systems for Real-Time Feedback Control of Reactive Ion Etching," *J. of Vacuum Sci. and Technol. B*, **14**, 483 (1996).

Edgar, T., S. Butler, W. Campbell, C. Pfeiffer, C. Bode, and S. B. Hwang, "Automatic Control in Microelectronics Manufacturing: Practices, Challenges and Possibilities," *Automatica*, **36**, 1567 (2000).

Hamaguchi, S., and M. Dalvie, "Microprofile Simulations for Plasma Etching Surface Passivation," *J. of Vacuum Sci. and Technol. A*, **12**, 2745 (1994).

Hamaguchi, S., M. Dalvie, R. Farouki, and S. Sethuraman, "A Shock-Tracking Algorithm for Surface Evolution Under Reactive-Ion Etching," *J. of Appl. Phys.*, **74**, 5172 (1993).

Harriott, L., and J. Vasile, "Focused Ion Beam Secondary Ion Mass Spectrometry: Ion Images and End-Point Detection," *J. of Vacuum Sci. and Technol. B*, **7**, 181 (1989).

Heimann, P., and R. Schutz, "Optical Etch-Rate Monitoring: Computer Simulation of Reflectance," *J. of Electrochem. Soc.*, **131**, 881 (1984).

Heinrich, F., and P. Hoffmann, "Analysis and Control of Ion Beam Processing by Optical Spectroscopy," *Vacuum*, **44**, 275 (1993).

Huang, C.-C., "Optical Heterodyne Profilometer," *Optical Eng.*, **23**, 365 (1984).

Humphreys, R., N. Chew, S. Morgan, J. Satchell, and A. Cullis, "End Point Detection in Ion Beam Milling of $YBa_2Cu_3O_7$ Thin Films," *Appl. Phys. Lett.*, **61**, 228 (1992).

Katardjiev, I., "Simulation of Surface Evolution During Ion Bombardment," *J. of Vacuum Sci. and Technol. A*, **6**, 2434 (1988).

Katardjiev, I., "A Kinematic Model of Surface Evolution During Growth and Erosion: Numerical Analysis," *J. of Vacuum Sci. and Technol. A*, **7**, 3222 (1989).

Katardjiev, I., G. Carter, and M. Nobes, "Simulation of Erosion Induced Surface Evolution in Temporally and Spatially Dependent Systems," *Vacuum*, **38**, 999 (1988a).

Katardjiev, I., G. Carter, and M. Nobes, "The Modelling of Surface Evolution During Growth and Erosion," *Int. J. of Numerical Modelling: Electronic Networks, Devices and Fields*, **3**, 137 (1990).

Katardjiev, I., G. Carter, M. Nobes, and R. Smith, "Precision Modeling of the Mask-Substrate Evolution During Ion Etching," *J. of Vacuum Sci. and Technol. A*, **6**, 2443 (1988b).

Kim, J., W. Carr, R. Zeto, and L. Poli, "Reactive Ion Etching Techniques for Silicon Sidewall Angle Control in Microengineering," *J. of the Electrochem. Soc.*, **139**, 1700 (1992).

Klein, E., "Identification and Etch Depth Control of an Ion Milling Process," PhD Thesis, Univ. of Colorado, Boulder (2000).

Klein, E., and W. Ramirez, "Consideration of Local Shadowing and Ion Beam Voltage Effects in the Prediction of a Surface Evolving Under Ion Milling," *J. of Vacuum Sci. and Technol. A*, **18**, 166 (2000).

Klein, E., W. Ramirez, and J. Hall, "A Common-Path Heterodyne Profilometer for the In-Situ Monitoring of Ion Milling Etch Rates," *Rev. of Scientific Instrum.*, **22**, 2455 (2001).

Korbicz, J., Z. Fathi, and W. Ramirez, "State Estimation Schemes for Fault Detection and Diagnosis in Dynamic Systems," *Int. J. of Syst. Sci.*, **24**, 985 (1993).

Lostimolo, P., "Ion Milling Cures Wet-Etchant Woes," *Microwaves and RF*, **24**, 95 (1995).

Ramirez, W., *Process Control and Identification*, Harcourt, New York (1994).

Riza, N., "Scanning Heterodyne Optical Interferometers," *Rev. of Scientific Instruments*, **67**, 2466 (1996).

Smith, R., and J. Walls, "The Development of a General Three-Dimensional Surface Under Ion Bombardment," *Philosophical Mag. A*, **42**, 235 (1980).

Veillard, D., "Real-Time Tracking of the Head-Disk Separation Using Laser Heterodyne Interferometry. Part One: Instrumentation," *IEEE Trans. on Magnetics*, **29**, 3909 (1993).

Manuscript received Sept. 29, 2000, and revision received June 26, 2001.